Nanoscale

PAPER

View Article Online
View Journal

Cite this: DOI: 10.1039/d5nr01457c

On the properties and origin of mesopore morphologies in dealuminated Faujasite Y zeolites

Valentina Girelli Consolaro,[a,b] Virgile Rouchon,[a] Walid Baaziz,[b] Adam Hammoumi,[a] Tom Ferté,[b] Gerhard Pirngruber,[a] Maxime Moreaud[a] and Ovidiu Ersen *[b]

Faujasite Y zeolites (FAU-Y) represent one of the most important categories of heterogeneous catalysts. They are historically known for their crucial role in the refining industry, and they have growing potential for upgrading bio-based products today. However, the thermal stability, acidity, and molecular transport properties of the synthesized zeolite are not ideal for the intended process conditions, activity, selectivity and catalyst deactivation. Consequently, post-synthesis physical–chemical treatments, such as dealuminating treatments, are usually employed to design a more efficient material that combines stronger acidity, better stability, and hierarchical porosity. This material is referred to as Ultrastable Y (USY) zeolite. Nevertheless, the precise mechanisms of mesopore network formation and its relationship with the crystal structure and morphology remain poorly understood. Our research investigates the evolution of the porous system induced by the dealumination in FAU-Y zeolites. Here, we propose a classification, quantification, morphological description and formation scheme of the mesopores with an unprecedented level of detail, that is based on electron tomography data from the main steps of the dealumination process. Four main groups of pores are identified: (1) closed, isolated mesopores with more spherical shapes and diameters of 7–8 nm; (2) open intracrystalline channeling mesopores that often run along crystallographic orientations, vary in diameter, and whose morphology recall a mechanism of isolated mesopore coalescence; (3) intercrystalline mesopores with irregular shapes detected at the boundaries of twinned crystals, and (4) surface roughness. We finally observe that the localization and development of mesopores are associated with structural defects, such as stacking faults and twinning. These results allow us to consider a nucleation/diffusion mechanism for the mesoporous network within zeolite Y during dealumination and provide guidelines for identifying new pathways to optimize hierarchical zeolites.

Received 10th April 2025,
Accepted 8th September 2025

DOI: 10.1039/d5nr01457c

rsc.li/nanoscale

Introduction

Zeolites are a class of crystalline aluminosilicates constituted of interlinking TO_4 tetrahedral units, where the T-sites are occupied by either Si or Al atoms. The topological arrangement of tetrahedra leads to a structural porosity, termed as the microporosity (pores diameter < 2 nm). Zeolites bare a charge deficiency for every aluminum atom in the structure, which may be compensated by cations bound to the micropore surface. When these cations are protons, the zeolites become acids, which lends, together with the molecular shape selectivity of the micropore topology, the catalytic properties to zeolites. Employed as catalysts, the microporosity together with the typical size of a grain of zeolite (micron/submicron scale) leads to diffusion limitations, which affect the initial activity and promote the catalytic deactivation. Several strategies have then been adopted to circumvent this issue and develop an optimized material for catalytic applications.[1,2] On one hand, the research turned towards the synthesis of zeolitic nanocrystals with a reduced size which decrease the diffusion mean free path.[3] On the other hand, mainly due to the thermal instability of these nano-sized zeolites, the scientific community put effort in engineering a hierarchy-based porous material. As a result, a secondary pore network is then introduced within zeolites, as an antidote to mass transport issues, at the expense of the microporous volume, leading to both enhanced thermal stability and catalytic efficiency.[4–6] The methods to insert a mesoporous network, that is featured by pore diameters ranging between 2 and 50 nm, within the zeolitic microporous framework are classified in two categories:

[a]IFP Energies Nouvelles, Etablissement de Lyon, Rond-point de l'échangeur de Solaize – BP3, 69360 Solaize, France
[b]Institut de Physique et Chimie de Matériaux de Strasbourg (IPCMS), UMR 7504 CNRS – Université de Strasbourg, 23 rue du Loess, BP 43, 67000 Strasbourg, Cedex 2, France. E-mail: ovidiu.ersen@ipcms.unistra.fr

bottom-up and top-down.[7,8] The bottom-up approach represents a versatile technique since the size of the pores can be accurately controlled by making use of soft or hard templating agents (surfactants or carbon black particles) to shape the mesopores during the synthesis of the zeolites.[9–11] However, the organic fingerprint of the precursors may raise the cost and therefore prevent up-scaling. The top-down protocols, instead, are based on the demetallation of pre-synthesized zeolites. Despite the poor control over the size and shape of the mesopores compared to the bottom-up pathways and the possible partial loss of crystallinity, the top-down strategies are widely spread thanks to their affordability and ease of practice allowing feasible industrial upscaling. In this approach, mesoporosity arises from the removal of Si and/or Al atoms from the T-sites. For example, non-selective fluoride-mediated etching removes both Si and Al atoms from zeolite T-sites.[12] For zeolites with a high Si/Al ratio, silicon is preferentially extracted from the lattice using alkaline solutions in a process called desilication.[13] For zeolites with a low Si/Al ratio, the object of interest in this study, mesoporosity arises from the selective removal of aluminum through hydrothermal and acidic treatments.[14,15] Complex multi-scale pore network architectures originate during the demetallation and a combination of diverse techniques is necessary to extract the morphological descriptors that characterize the porous network.[4,16–20] Physisorption, thermoporometry, and positron annihilation lifetime spectroscopy (PALS) can assess the level of pore connectivity in hierarchically porous zeolites, however the indirect nature of these characterization methods makes it difficult to spatially situate the pores.[18,21] To access the size distribution, shape, and localization of these mesopores, gas adsorption and Hg intrusion are associated with transmission electron microscopy (TEM).[22,23] The real space visualization of the core of zeolites at the nanometric level by TEM reveales the intricacy of the hierarchically porous network and the irregularity of the pore geometry, which render classical morphological models for porosimetry and physisorption less suitable for quantification. Innovative TEM-based methods have been proposed in the literature and offer interesting insights into identifying pore bottlenecks and occlusions.[24] In any case, conventional TEM approaches provide 2D information that are not sufficient to precisely differentiate the types of pores (interconnected *vs.* isolated) and to reveal the 3D spatial extension of the pore architecture in zeolites. For this reason, electron tomography (3D TEM) arises as one of the most valuable techniques to directly retrieve morphological three-dimensional features in the real space at the nanoscale. Already applied for characterizing catalytic and porous materials,[25,26] 3D TEM has quickly become oriented toward investigating zeolite crystals and their secondary pore generation,[27,28] with particular attention given to the mesopores volume, shape and size in hierarchical demetallated zeolites of the Faujasite (FAU) type Y.[4,19,29–31] According to previous works, the main results of dealumination in FAU Y zeolites are isolated cavity-like and cylindrical interconnected pores with diameters of 15–30 nm.[29] Other products, such as extra-framework aluminum (EFAL) species, which are presumably generated during hydrothermal steps and subsequently removed from the material *via* acid attack, have also been observed. The evolution of the mesoporous system from its origin to the final interconnected pores, together with the nature of the EFAL species, are still questioned, though. Specifically, what remains unclear is (i) where and at which stage of the dealumination the zeolite microstructure begins to rearrange to accommodate the mesopores, (ii) what are the intermediate steps in terms of pores network architecture before reaching the final optimized material, and (iii) where does the material expelled from the crystalline sites accumulates. Finally, the relationship between the shape of the mesopores and the structural properties of the crystals is not well established and requires investigation. Keeping these questions in mind, within a multi-step protocol starting from the microporous FAU Y zeolite and ending with the mesoporous USY zeolite, our research considers the role of each controlled dealuminating step in the expansion of the secondary pore system. To characterize the pores, we designed and quantified descriptors retrieved by 3D TEM data and mathematical morphology-based data processing. In conclusion, by combining electron tomography, electron diffraction and gas adsorption we aim to explore with an unprecedented level of detail the inherent relationship among the morphology, the topology and the structure in Y zeolites during the evolution of the pore network at the nanometric scale and propose a mechanism of dealumination.

Materials and methods

Preparation of FAU Y samples

To introduce mesoporosity *via* dealumination, hydrothermal and chemical treatments were performed on the commercially available $NaNH_4$ Y zeolite (Zeolyst®), also termed CBV300. This parent zeolite has a unit cell of 24.7 Å, associated to Si/Al ratio by XRD of 2.7, and % Na content of 1.61 ppm (by ICP). Additional information on the CBV300 is found in the SI. The protocol for dealumination from the CBV300 zeolite was articulated as follows: low temperature steaming (steaming 1), ion exchange, high temperature steaming (steaming 2) and acid leaching.

Steaming 1. 25 g of zeolite CBV300 were placed in a tubular quartz reactor. The reactor was placed in the furnace, and the zeolite heated at 5 °C min^{-1} with a dry air flow of 0.2 L $(h\ g)^{-1}$ zeolite until reaching 620 °C. At 300 °C, water was inserted in the reactor with a flow rate of 0.8 L $(h\ g)^{-1}$ zeolite to obtain a treatment under 80% steam and 20% of dry air on a molar basis. The temperature of 620 °C was held for 2 h, then the system was cooled down overnight. The water flow rate was maintained throughout the treatment and only ends when the temperature reached 265 °C.

Ion exchange. A solution of NH_4NO_3 (VWR Chemicals, NH_4NO_3 > 98.5%) was prepared for the exchange step. The steaming 1 zeolite was suspended into 4 M of NH_4NO_3 so that V/m = 10 mL g^{-1} zeolite. The suspension was refluxed for 4 h

under stirring, filtered and washed four times with distilled water *via* centrifugation. Then, it was dried overnight at 100 °C. The ion exchange was performed 3 times.

Steaming 2. Experimental settings as for low T steaming, with maximum temperature set at 700 °C, were performed on the *ionic exchange* zeolite.

Acid leaching. The steaming 2 zeolite was suspended into 1 M of HNO_3 (Fisher Scientific, HNO_3 at 60% w/w solution in water) solution so that V/m = 5 mL g^{-1}. The suspension was heated at 90 °C for 2 h under stirring, filtered and washed four times with distilled water *via* centrifugation. Finally, it was dried overnight at 100 °C.

N_2 physisorption

Analysis were performed on the Micromeritics Physisorption Analyzer ASAP 2420. The total pore volumes were obtained from the volume of nitrogen adsorbed at the relative pressure of 0.99 and the microporous volumes by t-plot method. Specific surface areas are calculated according to the Brunauer–Emmett–Teller (BET) method using data points in the relative pressure (p/p_0) range of 0.05–0.30. The PSD curves derived from the adsorption and desorption branch were estimated with the Barrett–Joyner–Halenda (BJH) model and the corrected Kelvin equation on the adsorption and desorption branches for the range of 2–50 nm of pore diameters.

X-Ray diffraction

Analysis were performed using a PANalytical X'Pert Pro Diffractometer in Brag-Brentano configuration with Cu Kα radiation (λ = 1.54 nm) fitted with Miniprop detector. For the data acquisition the powder of the sample was compacted in a sample holder. An angle range of 2° to 70° 2θ with a step size of 0.02°, dwell time of 5 s per step were set for the measurements. The assignments of the crystalline phases were carried out using DIFFRAC.TOPAS software. The following information file was used for the phase identification: PDF 00-038-0239 for the Faujasite-Na zeolite.

Scanning electron microscopy

Imaging is performed on a Zeiss GeminiSEM 500 equipped with a field emission gun. Primary electrons are accelerated with 0.7 kV. The images are obtained by secondary electrons with In-Lens detector at a working distance of 1.8 mm. The zeolite was dispersed into ethanol and the solution drop-casted on aluminum stubs.

Transmission electron microscopy

A droplet of solution containing gold nanoparticles of 5 nm diameter (Sigma Aldrich, suspension in 0.1 mM PBS reactant free) was deposited on a TEM copper grid coated with a holey carbon film. The powder of zeolite was dispersed into ethanol and then sonicated for 10 min. 1–2 droplets of this suspension were drop casted on the same TEM grid. TEM measurements were performed on a JEOL 2100F operated at 200 kV and equipped with a probe corrector for spherical aberrations. For the STEM images, the electron probe was 0.1 nm and the series of tomographic projections were acquired in ADF-STEM mode using a camera length of 12 cm. The STEM images have a resolution of 1024 × 1024 pixels and are acquired with a dwell time of 15 µs per pixel and a beam current of 35 pA.

Electron tomography (3D TEM)

For every STEM projection, the defocus, the horizontal specimen shift and specimen tilt were controlled automatically *via* the Tomography plugin of the Digital Micrograph software by Gatan. The goniometric parameters of tilting and increment steps for the electron tomography series are reported in SI. The alignment of the tilt series was performed by the IMOD software (v4.11)[32] and the reconstruction is carried out with the TomoJ plugin (v2.8.1)[33] of ImageJ (v1.54) by SIRT algorithm (100 iterations with a relaxation coefficient set at 2). The segmentation and volume rendering make use of the software 3D Slicer (v4.3.0).[34] Videos of all the reconstructions and volume renderings can be found in the supporting material.

Computation of the morphological and geometrical descriptors

Multi-step protocols on ImageJ and plug im! softwares were specially developed or applied for quantifying the listed morphological descriptors on the segmented volumes.[35,36] More details are found in SI.

Results and discussion

The demetallation steps employed in this study consist of a first hydrothermal treatment (steaming 1), an ion exchange, a second hydrothermal treatment (steaming 2) and an acid leaching. More details on the sample preparation and experimental conditions of dealumination are reported in the dedicated section of Materials and methods. The role of each dealuminating treatment is described through electron microscopy-based characterization techniques. The secondary electron SEM imaging analysis qualitatively shows the localization of the mesopores and related surface features. The TEM analysis, mainly based on 3D TEM and image processing adds quantitative information on the structure and the morphology of typical grains of zeolite Y and their porous networks. Specifically, the 3D TEM identifies the family of the mesopores and aims to provide, in association with N_2 physisorption measurements, the most suitable descriptors for mesoporous materials. Using this approach, we are able to quantify morphological parameters such as the porous volume and the pore size distribution, and geometrical elements like the pore sphericity and the bottleneck diameter. These results are summarized in the paragraphs describing the classification of the mesopores, the morphological and topological parameters. A further paragraph combines the findings for each category in order to elucidate the mechanism of the mesoporisation by demetallation.

Family of mesopores in typical Y grains

Single grains of Faujasite Y zeolites are described as octahedron-shaped particles with {111} facets, and other sym-

metries for the vertices.[37,38] In this study we have investigated Y zeolite crystals of hexagonal prisms geometry (irregular octahedron) as depicted in Fig. 1a (and in Fig. S1). According to the SAED pattern of Fig. 1b, the lateral facets are indexed as {111} for the reciprocal distance $1/d$ at 1.50 nm^{-1} (purple circles in Fig. 1b). The basal surfaces are also labelled as {111} (Fig. 1c). Other families of plans describe the corners. Among these, recurrent $1/d$ at 1.31 and at 2.04 nm^{-1} are imputed to the {311} and {511} symmetries, respectively. By observing the redundancy of this typology of Y grains, 3D TEM measurements were performed on samples alike. Therefore, in such grains four categories of mesopores are identified (Fig. 1e). The first category is constituted of the isolated mesopores inside the microporous matrix. Already described in remarkable works,[29–31] the isolated mesopores (in orange in Fig. 1e) access the external surface and the neighboring mesopores through framework micropores only. Contrarily, the open mesopores directly access the external surface. In the current study, the remaining three categories (in blue in Fig. 1e) belong to the open mesoporosity. These have been termed: the intracrystalline channeling mesopores, the intercrystalline mesopores and the surface roughness. While the intracrystalline channeling mesoporosity is typically crossing the grain from the edges to the core, the intercrystalline mesoporosity is found at the interface of twinned grains. All other elements which are not identified as isolated mesopores, neither channeling nor intercrystalline mesopores, are located on the external surface and ascribed to surface roughness. The starting material, CBV300 Y zeolite, is a nearly exclusive microporous sample with smooth facets, as confirmed by the TEM and SEM images in the SI (Fig. S2 and S3). Before post-treatments, no mesopores are observed inside the zeolite and only a few ones are present on the external facets. This suggests that the pre-existing pores are only superficial. Also noticeable at the level of the parent zeolite are intergrown crystals and stacking faults, presumably defects of synthesis. After the first steaming, isolated mesopores, intercrystalline mesopores and surface roughness are observed (Fig. 2a and e). Interestingly, the slices of Fig. 2b–d of the tomographic segmentation show a higher concentration of isolated mesopores that form parallel arrays to both lateral (light blue and rose arrows) and basal (yellow arrow) facets. Moreover, these mesopores are found on a stacking fault surface (Fig. 2b), as one could deduce by the mirror symmetry of the lateral facets in correspondence to this

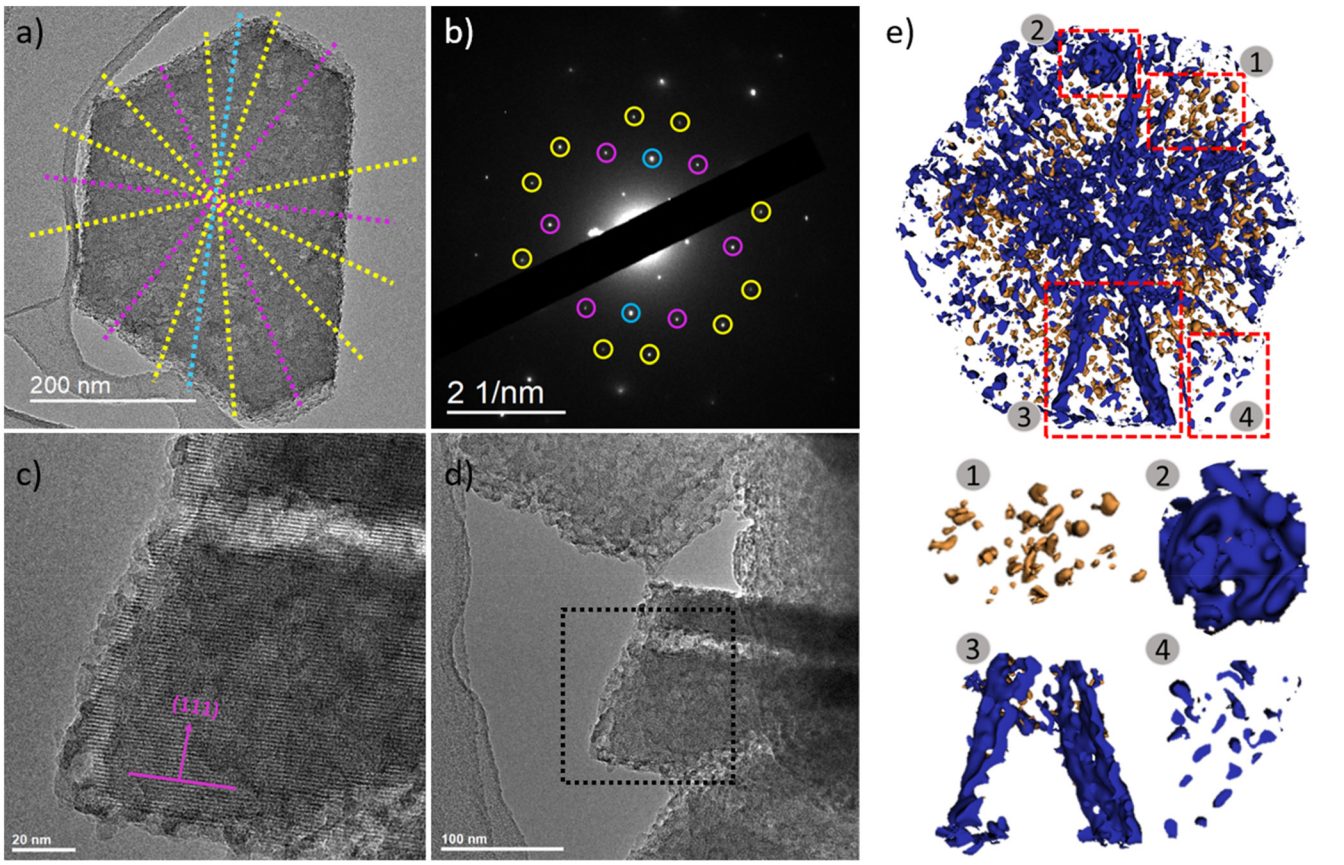

Fig. 1 Typical octahedron shaped Y zeolite (after ionic exchange) with hexagonal base observed by TEM (a). The SAED pattern of (a) with related symmetries (b). The purple cercles refer to the [111] directions which label the lateral facets, the blue to the [311] and the yellow to the [511] both describing the corners. The HRTEM micrograph showing also the (111) labelling (c) and the full field area for a steaming 2 zeolite (d). Mesopore network 3D rendering of a steaming 2 zeolite (e). The closed mesopores are depicted in orange (1), whereas the open pores accounting for intercrystalline mesopores (2), intracrystalline channelling mesopore (3) and surface roughness (4) are depicted in blue.

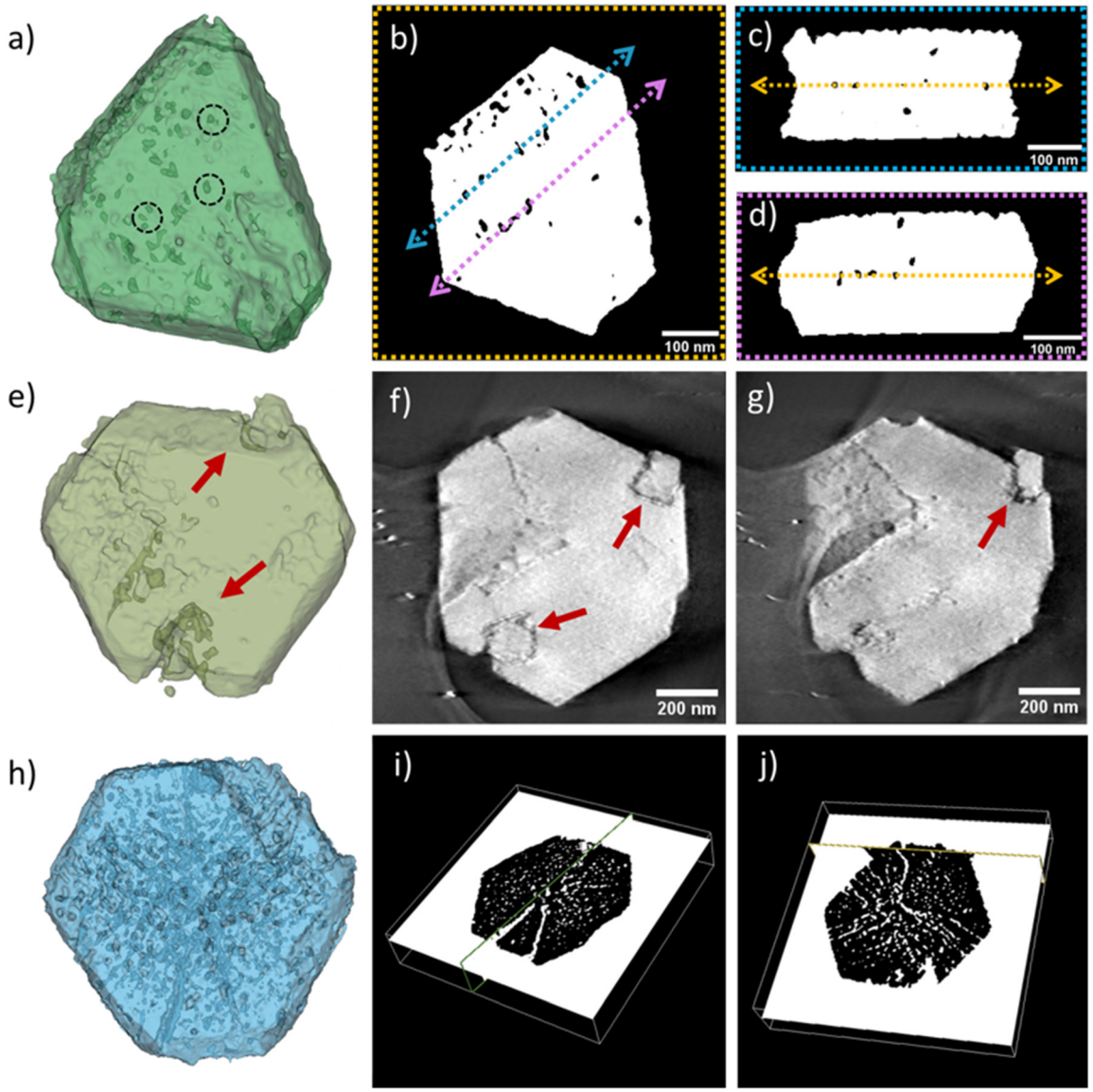

Fig. 2 3D volume of a steaming 1 zeolite (a) and associated segmented sections of its reconstruction (b–d). The black dotted circles highlight the presence of closed mesopores. The double arrows show where the slices are cut into the grain. 3D volume of another grain of steaming 1 zeolite (e) and associated sections of reconstruction (f and g). In this case, the sections are parallel to the basal surfaces and the red arrows point to the sites of the intercrystalline mesoporosity. 3D volume of a steaming 2 zeolite (h) and its segmentation (i and j). The extracted cross sections illustrate the propagation of the intracrystalline channeling mesopores and their preferential orientations.

surface (yellow arrow in Fig. 2c and d). The slices of the reconstruction in Fig. 2f and g referring to the zeolite in Fig. 2e, illustrate the existence of intercrystalline mesopores between the principal crystal and two smaller intergrown twinned crystals, pointed out by red arrows. One could notice the irregular shape of this type of mesopores, which circumscribe these secondary grains. At more advanced stages of the dealumination, all four categories of mesopores are exhibited, including the channeling mesopores. This is the case for the grain after steaming 2 of Fig. 2h–j, whose mesoporous network is depicted in Fig. 1e. In Fig. 2i, the channels are spreading parallel to the basal surfaces, and it is possible to identify some frequent directions of propagation: either from the corners or from the middle of the facets towards the core of the crystal. Sometimes, they cross the zeolite throughout its whole thickness, as it is possible to appreciate in the 3D rendering of Fig. 1e and in the cross section of Fig. 2j. To corroborate this observation, additional slices are reported in Fig. S4, where the channeling mesopores seem to be cutting the zeolite into several fragments. In contrast to these classes of open porosity involving large pores with above-listed shapes, the surface roughness is mainly composed by smaller pores localized at the edge of the crystals and characterized by diverse morphologies (Fig. 1e). Its qualitative description can be easily

retrieved through the 3D rendering of the mesoporous network and the imaging by SEM (Fig. 3a and b). However, a quantitative approach to outline the surface roughness is less trivial (and less accurate) due to the presence of artefacts on the reconstruction by 3D TEM of the zeolite grains' external surface. Finally, the SEM and HRTEM micrographs in Fig. 3 illustrate the presence of mesopores with access to the surface and structural anomalies, such as twinning and stacking faults, in dealuminated zeolites. These micrographs reveal a correlation between the localization of open mesopores and structural defects. The latter were already noticed in the pristine material.

Morphological parameters: porous volume and pore size distribution (PSD)

Based on the nitrogen physisorption data, the microporous volume V_μ is associated to the largest fraction of the porosity within zeolites (Fig. S5, S6 and Table S1 of the SI). Before any treatment, the commercial sample CBV300 is featured by a total porosity of 0.379 $cm^3\ g^{-1}$, for which V_μ is imputed to 0.332 $cm^3\ g^{-1}$. After the first steaming the porosity is shared as it follows: V_μ occupies 0.270 $cm^3\ g^{-1}$ and the mesoporous volume V_M measures 0.108 $cm^3\ g^{-1}$. When the ionic exchange step is performed, both V_μ and V_M raise to 0.321 $cm^3\ g^{-1}$ and 0.141 $cm^3\ g^{-1}$, respectively. At the end of the second steaming, V_μ drops to 0.259 $cm^3\ g^{-1}$ while V_M keeps rising and reaches 0.200 $cm^3\ g^{-1}$. In the final stage of the dealumination, that is when the acid leaching is completed, V_μ is 0.289 $cm^3\ g^{-1}$ and V_M has grown to 0.243 $cm^3\ g^{-1}$. With the exception of the pristine zeolite, here reported only as a reference in terms of initial porosity, the porous volumes extracted from the N_2-physisorption analysis for the different zeolites are compared in Fig. 4a. In addition, from the isotherms (Fig. S5 of the SI) we can estimate the rate of closed mesopores. This fraction of porosity supposes a cavitation effect and is concretely obtained as the difference between the adsorbed volume on the adsorption branch before the hysteresis, which is between $0.4 < p/p_0 < 0.5$, and the adsorbed volume on the desorption branch at the lower p/p_0 step in the hysteresis loop.[39] Therefore, the portion occupied by the closed mesopores during the dealumination results in: 0.006 $cm^3\ g^{-1}$ for steaming 1, 0.015 $cm^3\ g^{-1}$ for ionic exchange, 0.024 $cm^3\ g^{-1}$ for steaming 2 and 0.032 $cm^3\ g^{-1}$ for the acid leaching. If related with the total mesoporosity, these values represent in percentage the 5.5%, the 10.6%, the 12.0% and the 13.2% of V_M, respectively. Complementary to the results from physisorption, V_M is directly extracted from the 3D TEM data at the single crystal level (Fig. 4b). For each of the four stages of the dealumination, two zeolites' crystals

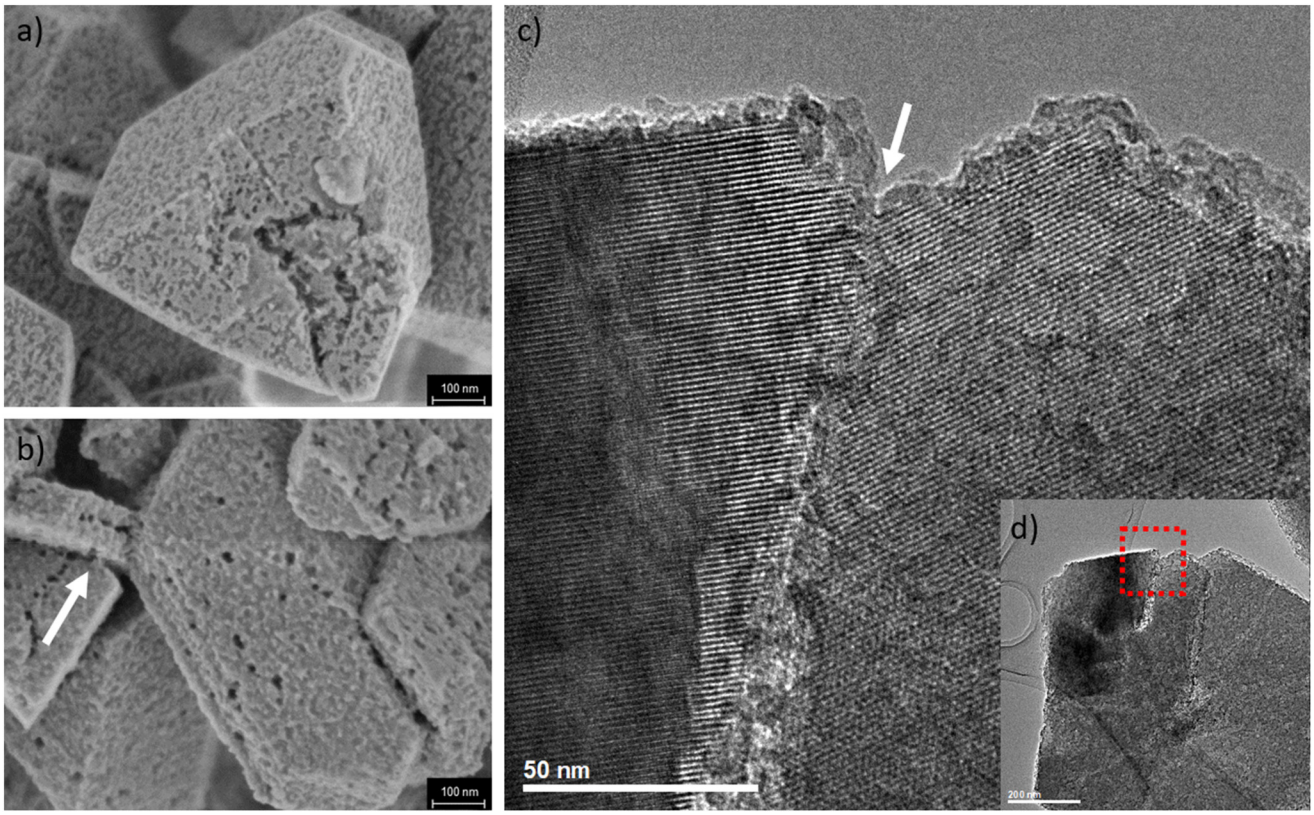

Fig. 3 SEM images of steaming 1 (a) and acid leached zeolites (b). The surface roughness and the mesoporosity between twinned crystals is already present at the early step of the dealumination. HRTEM micrograph illustrating the presence of a stacking fault in a steaming 2 zeolite (c) and the full field area (d). At more advanced stages in the treatment, such as after a second hydrothermal treatment or a leaching, the mesopores furtherly concentrate on stacking faults (white arrows).

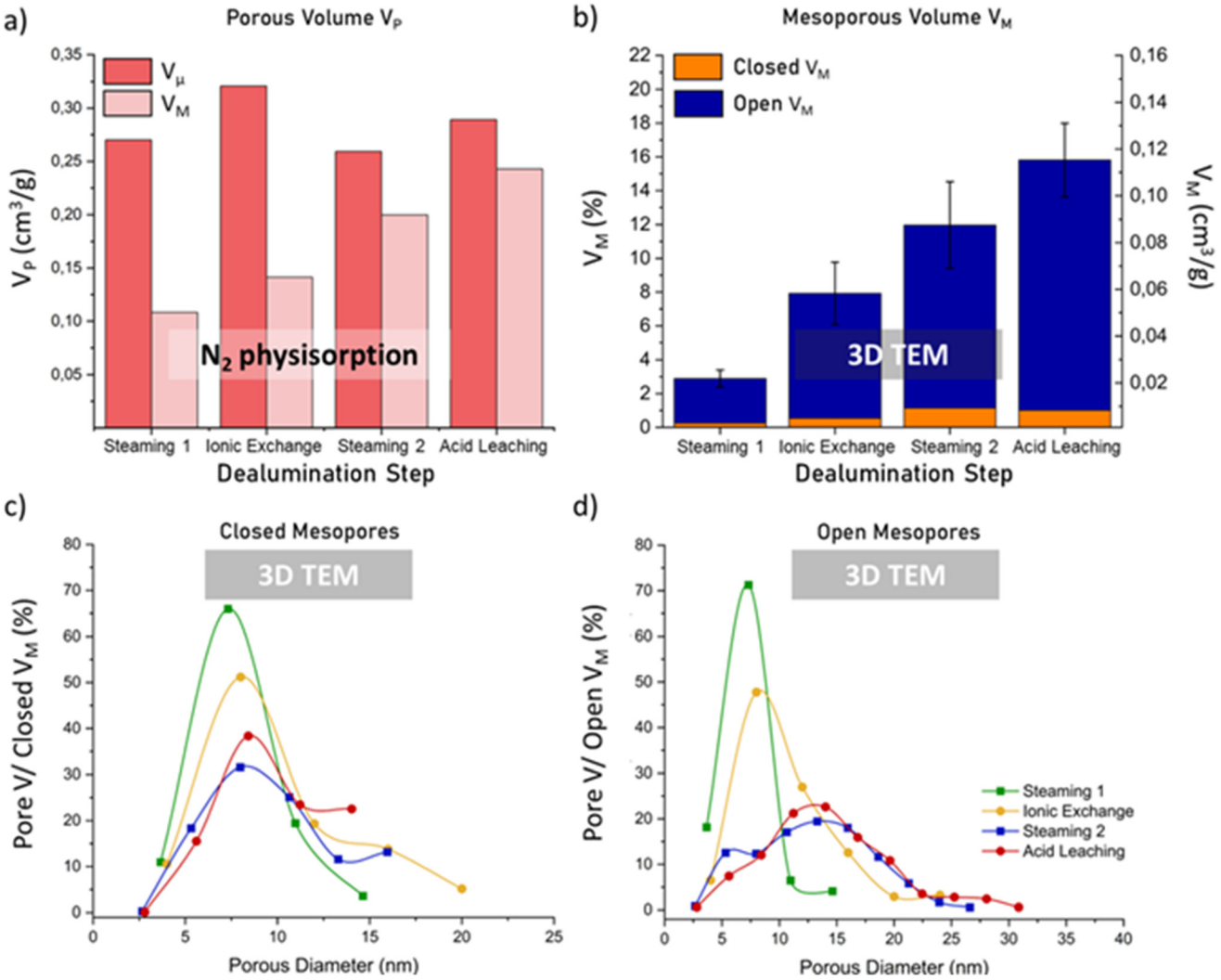

Fig. 4 Microporous (V_μ) and mesoporous (V_M) volumes obtained by N_2 physisorption (a). The sum of V_μ and V_M results in the total porous volume that is accessible during the adsorption and desorption. Mesoporous volume obtained by 3D TEM on individual grains as the sum of the closed (orange) and open (blue) mesoporous volume (b). The discretized PSD derived from 3D TEM for both closed (c) and open (d) porosity along with the dealumination steps.

representing the typical grains according to the description provided in the previous paragraph (and shown in Fig. 1a and b), were chosen for the electron tomography measurements. The mesoporous volume is therefore obtained by image processing on the 8 segmented zeolite reconstructions, however, given the size of the zeolite crystals, the spatial resolution does not allow to track the micropores since the pixel (or voxel) resolution is ≈1 nm (or 1 nm^3). Furthermore, when V_M is retrieved from 3D images, it is returned in voxel units, *i.e.* either in nm^3 or as a percentage of the whole volume of the zeolite. For this reason, we have converted V_M into the common unit of volumes for porous materials, by considering the structural density of Y zeolites equal to 1.37 g cm^{-3}, as expressed in the literature.[40] Thus, V_M evolves from (0.021 ± 0.004) cm^3 g^{-1} after steaming 1 (corresponding to 2.9 ± 0.5% when normalized to the total volume of the zeolite), to (0.058 ± 0.014) cm^3 g^{-1} after ionic exchange (7.9 ± 1.8%), keeps rising up to (0.088 ± 0.019) cm^3 g^{-1} after steaming 2 (12.0 ± 2.6%) and at the end of the HNO_3 leaching step it reaches (0.115 ± 0.016) cm^3 g^{-1} (equivalent to 15.8 ± 2.2%). In this case, given that the analysis is performed on a limited number of samples, the error associated with the averaged value corresponds to the deviation from the mean. The closed and open mesopores can be easily visualized (Fig. 1e) and calculated. The reader will find more details about the image processing methodology in the SI. The closed V_M for instance is estimated 0.002 cm^3 g^{-1} at steaming 1 (equivalent to 9.5% of the mesoporous volume), 0.004 cm^3 g^{-1} at ionic leaching (6.7% of V_M), 0.008 cm^3 g^{-1} after steaming 2 (9.1% of V_M) and 0.007 cm^3 g^{-1} (6.3% of V_M) at the fully dealuminated stage. These porous contributions are shown in Fig. 4b. Although the mesoporous volume occupies a smaller portion of the total porous volume, by comparing the results from both techniques, it is possible to confirm the rising trend of V_M, mainly due to the fraction of

open mesopores. Once the pores classifications and volumes are provided, it is interesting to describe the mesopores by their diameter distribution. The PSD is classically derived by N_2 physisorption measurements. In this case, the BJH method was employed to obtain the PSD plots in Fig. S6. The diameter distribution in the adsorption branch illustrates a single population of pore size peaking around 7 nm (steaming 1) and around 10 nm (ionic exchange). A bimodal distribution (at least) features the samples after steaming 2 with a first peak around 7 nm and a second broad one around 15 nm. For the leached zeolites, while the first pores population keeps unvaried, the second one has shifted towards a mean diameter of 22 nm. However, despite the important information that can be extrapolated from these PSD data, the physisorption is an indirect technique that supposes geometrical assumptions in terms of pores morphology. Thus, the realistic shape, size and localization of the mesopores remain still unclear. To get a better insight into the spatial distribution of the different pores size populations, four grains of zeolites (among the eight volumes) were selected, that is one volume for every step of the dealumination. Here, the PSD is extracted with protocols of image processing that are detailed in the SI. In order to keep a distinction between the main classes of mesoporosity, the PSD is computed for both the closed and the open mesopores, as we show in Fig. 4c and d. From the graphics, we observe that the pores introduced during the first two treatments are characterized by a monomodal pore diameter distribution, with a maximum between 7–8 nm diameter. This is valid for both the open and closed mesopores. For the two further steps in the demetallation process, while the closed mesopores are still marked by a PSD between 7–8 nm, the open pores exhibit a multimodal size distribution. Within the zeolite after steaming 2, broad size distributions are found for diameters of 5 and 13 nm. Within the zeolite after leaching, a minor population around 5 nm diameter is followed by a smooth main population at 14 nm and a tail between 25 and 30 nm diameter. The graphical representation of the zeolites and their open pores from the ion exchange to the HNO_3 final leaching is given in Fig. 5a–f. No intercrystalline mesopores are observed in these three zeolites, which means that the PSD for the open porosity refers exclusively to channeling mesopores and surface roughness. In this intricate pore network, as

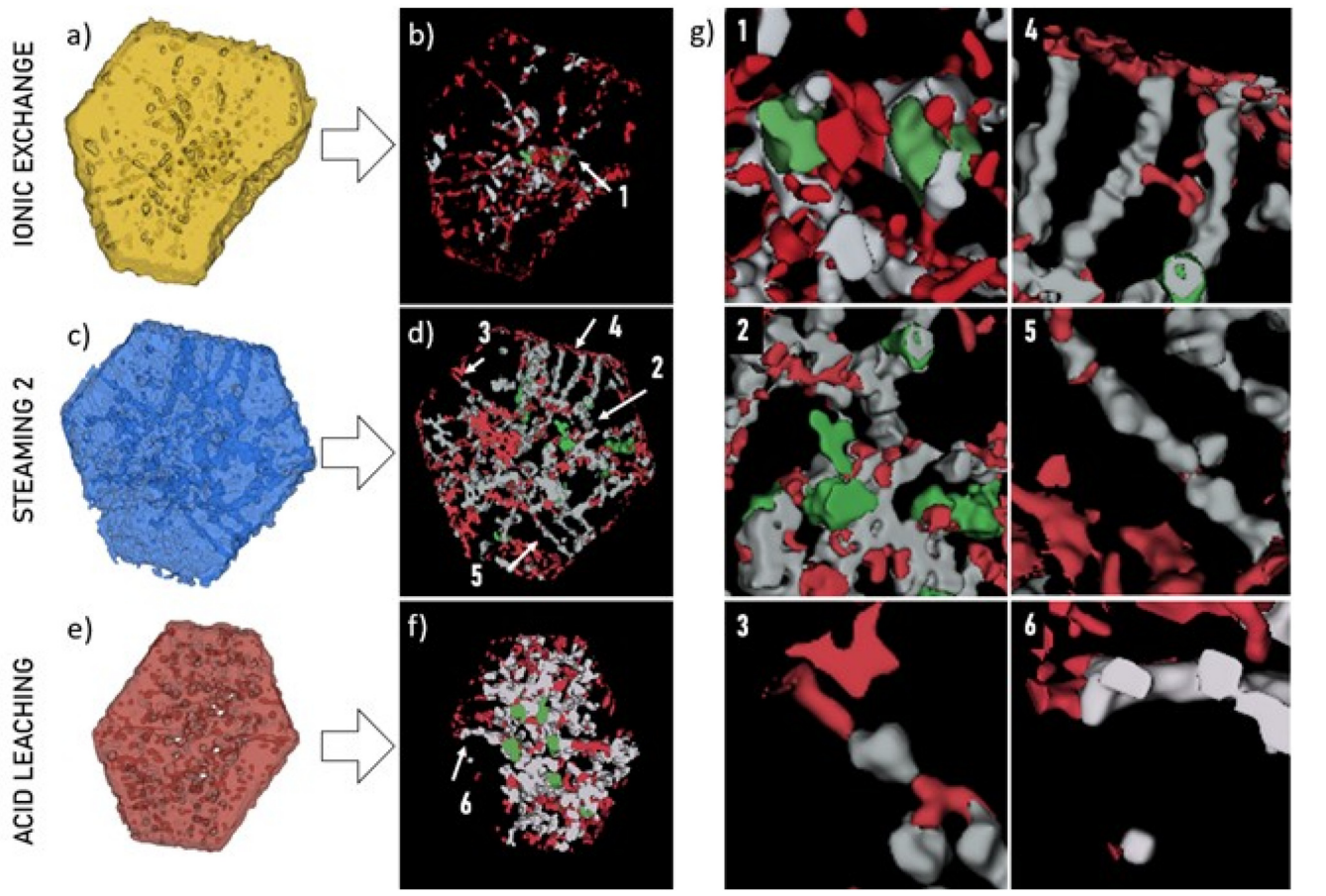

Fig. 5 3D volumes of zeolites used for the 3D TEM analysis after the ionic exchange (a), the steaming 2 (c) and the leaching (e) and their corresponding 3D rendering of the mesopores network (b, d and f). The PSD of the open mesopores is divided here into three ranges (g): red ($d \leq 8$ nm), grey ($8 < d \leq 20$ nm) and green ($d > 20$ nm). The zoomed renderings from 1 to 6 of the mesopores correlate the pores morphology with their sizes.

we observe in Fig. 5d–f, the whole distribution of diameters has been divided into three intervals, each of them assigned to a color code. If the diameters $d \leq 8$ nm the pores are shown in red, if $8 < d \leq 20$ nm in gray and if $d > 20$ nm in green. After the ion exchange step, almost the entire network of open mesopores falls into the $d \leq 8$ nm class. For the steaming 2 and for the acid leaching, the smallest range is attributed to the external roughness, the external mouths of the channeling mesopores, the pore throats and the pore branching. This range corresponds to the first pore population that was observed in the graph of Fig. 4d. Larger diameters in the range of 8–20 nm are attributed to the body of the mesopores, and they constitute the broader peak in the PSD plot. Finally, within the steaming 2 and the leached zeolites, the interval of diameters above 20 nm characterizes the largest void fractions due to the coalescence of the channeling mesopores. These elements forming the tail of the PSD graph are located close to the crystal core. Not only the electron tomography describes a similar PSD such as the BJH method, but in addition it maps in 3D the spatial relationship between size populations of pores. Therefore, according to the 3D TEM results, the PSD does not refer only to different types of open porosity but additionally indicate that different diameters correspond to different portions of the same mesopore. Ergo, a typical channeling mesopore is described by a narrow mouth, a larger body (with possibly narrower throats and secondary branching), and a potentially even larger bulge towards the core of the zeolite, where it could merge with other porous entities. Some examples of these pore features are portrayed in the cropped frames of Fig. 5g, listed from 1 to 6.

Geometrical parameters: sphericity, overlapping factor and bottleneck diameter

A qualitative analysis on the morphology of the mesopores is provided in Fig. 6. From the slices of the tomographic reconstructions, one could notice that rounded mesopores characterize the grain after the first steaming (Fig. 6a and b). After the ion exchange (Fig. 6c and d) both rounded and elongated intracrystalline mesopores are observed. It is interesting to note in the crop of the reconstructed slice that the intracrystalline channeling mesopore is apparently shaped by rounded porous units of regular diameter, recalling 'pearls in a necklace'. These porous units spatially follow one another and merge on the plane parallel to the hexagonal base (xy plane) along a direction of elongation, in this case from the middle of the facet to the core of the grain. This configuration is made more irregular and entangled after steaming 2, where the directions of elongation branch out (Fig. 6e and f). At this stage, the channeling mesopores are numerous. They can run on the (xy) plane along several directions, and sometimes they intersect even before reaching the center of the zeolite. When the leaching is performed, the geometry of the channeling mesopores gains in regularity (Fig. 6g and h). Even if porous units with rounded morphologies are still observed in shaping the channel, the pore walls look smoother. With all due precaution, we might claim that after the leaching step, the pore

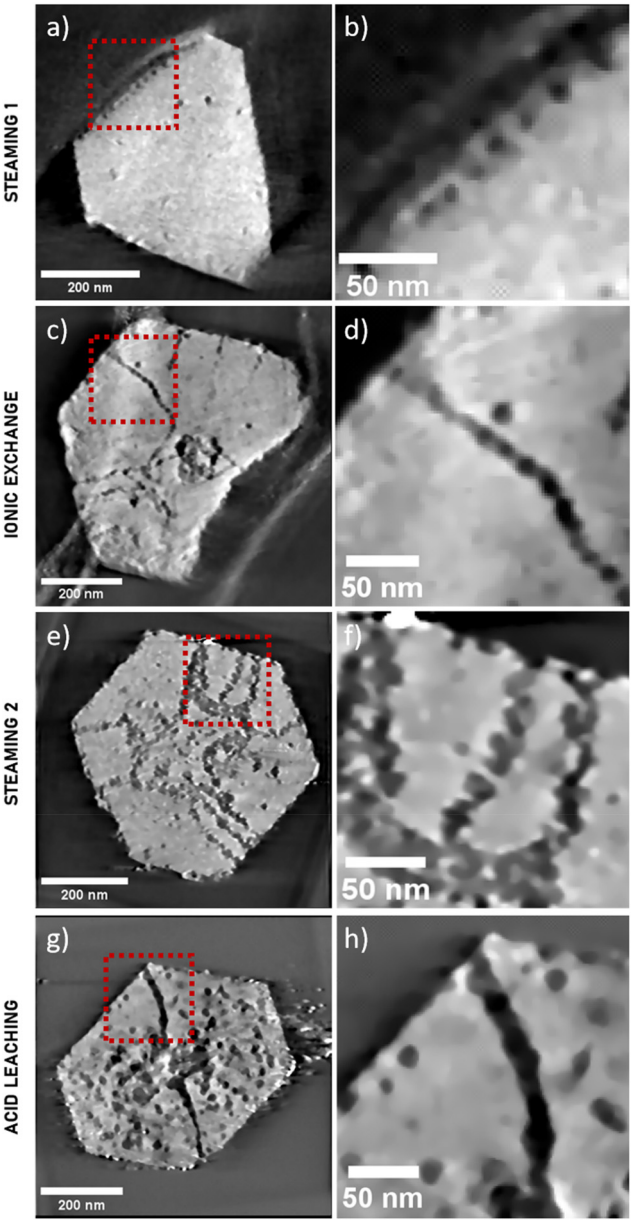

Fig. 6 Reconstructed slices monitoring the evolution and propagation of the mesoporous morphology within the zeolites at the four steps of the dealuminating treatment: after steaming 1 (a and b), ionic exchange (c and d), steaming 2 (e and f) and acid leaching (g and h).

geometry tends to a cylinder (Fig. 6h) instead of a necklace. Thus, to describe this evolution *via* a more quantitative approach, three geometrical descriptors were extracted from the tomographic volumes. The chosen parameters are the pore sphericity, the overlapping factor and the bottleneck diameter. The first one accounts for the degree of anisotropy of each mesopore and is a function of the pore' surface and volume according to eqn (1) in the SI. Based on its definition, each mesopore can be classified in one of the five categories of the sphericity ϕ ranging from a very low (ϕ close to 0) to a very high (ϕ close to 1) spherical class.[41] The results for the sphericity, which are reported in Fig. S7, show that all along the deal-

umination the closed mesopores are populating classes of higher sphericity than the open mesopores, and are characterized by a constant mean volume. Contrarily, the open mesopores populate the least spherical classes and are associated to an increasing mean volume during the dealuminating treatments. The second parameter, the overlapping factor h/R is introduced to detail the peculiar configuration of the open channeling mesopores. The overlapping factor is based on the hypothesis that the pore morphologies can be described by arrays of variously intersecting spheres forming extensive lengths, recalling the 'pearls in a necklace' analogy. Mathematically, h/R consists of the ratio between the overlapped distance between two spheres and their radius, and it assumes that the porous units are spheres of equal radius. Its value is ranged between 0 and 1 (boundary conditions), where 0 means that the porous units are totally disconnected, and we do not longer observe a channel, and 1 that the porous units are integrally intersecting, and the shape of the channel tends to a cylinder. Finally, the bottleneck factor a/R describes the degree of narrowing in a channeling mesopore. In this case, a corresponds to the smallest radius (*i.e.* the bottlenecking radius) that is measured at the intersection between the two spheres of radius R. Similarly to the overlapping factor, also a/R is bound between the limit values of 0 and 1. More details on the mathematical formulation of these two parameters h/R and a/R and their reciprocal relation are found in eqn (2) and (3) of the SI, together with schematic illustrations (Fig. S8 and S9). It is worth mentioning here that both the overlapping and the bottlenecking factor were analytically retrieved by knowing the PSD, the surface area and the volume for each mesopore. By considering the porous network of Fig. 5, the computation of h/R and a/R has been realized for 5 to 8 channeling pores (or pores' fraction) per zeolite with homogenous R. These results are summarized in Fig. S10 of the SI. After the ion exchange, h/R is 0.3 ± 0.2 and a/R is 0.7 ± 0.2, meaning that for a typical pore diameter of 8 nm such as the one obtained by image processing PSD (Fig. 4d), the bottleneck diameter is 5 ± 1 nm. In steaming 2, h/R decreases to 0.2 ± 0.1 and the bottlenecking is 0.5 ± 0.2, leading to a constriction of 6 ± 2 nm in size within a pore with a steady diameter of 13 nm. For the acid leached zeolite, the overlapping factor rises again to 0.3 ± 0.2 and a/R results in 0.6 ± 0.3, for which the bottleneck reaches 8 ± 3 nm diameter for a channeling mesopore of 14 nm diameter. Although this method can present some approximations, since both the pores surface and volume are considered in a discretized space of voxels, it provides for the first time a description of the bottlenecking effect that is based on real space data and direct measurements and is recurrent over the whole length of channeling mesopores.

Mesopore formation and evolution during dealumination

Pore nucleation. The isolated mesopores of 7–8 nm diameter, together with intercrystalline mesopores (and surface roughness) are observed already at the earlier stage of the dealumination. In particular, the intercrystalline mesopores are found along the edge of the facets, while the isolated mesopores are heterogeneously distributed throughout the core of the zeolite. Specifically, a higher density of isolated mesopores is observed within the internal surfaces of Fig. 2b–d. These mesopores align parallel to the basal and lateral facets respectively, which presumably belong to the {111} symmetry. Moreover, from the cross sections we notice that at least one of the internal surfaces (highlighted with yellow arrows) shows the typical features of a defective plane. Through the morphology of the lateral facets, characterized by a twinned profile orthogonal to the basal plane, we have attributed it to a stacking fault surface. Two aspects of such closed mesoporosity can be highlighted after the initial hydrothermal treatment. Firstly, arrays of isolated mesopores are found along the intersection of planes parallel to facets, *i.e.* at the crossing of {111} surfaces. Secondly, a higher concentration in specific portions of the zeolite may be associated with pre-existing defects, in this case at a defective 2D surface. Some examples of the intercrystalline mesoporosity are provided in Fig. 2e–g and in Fig. 3. These mesopores are spatially extending at the interface of intergrown twinned grains, literally delimiting the surface in between. Since the microporous matrix is cleaved at these grain boundaries, the intercrystalline mesopores present an irregular morphology that retraces the crystal surface. These results suggest that the removal of the microporous matrix after a single hydrothermal step often occurs in regions where defects from the process of synthesis of the material, such as stacking faults or twinning, preexist. This assumption is corroborated by previous studies, where the role of defects as triggering sites of mesopores nucleation was investigated for different families of zeolites. In Beta zeolites (BEA) the dealumination starts at specific T-sites and the mesopores extend on the most defective plane (which are the (001) in BEA) where stacking faults are concentrated.[42] In the MFI and FAU topologies, the mesoporosity is associated to twinning planes, that are supposed to be less stable than the non-twinned ones, and to intergrowths.[38,43–45] Even for mesopores derived from NH_4F-based etching solution, the grain boundaries and the intergrown crystalline polyhedrons in Y zeolites are considered to be the preferential sites to remove material, because of the strain of the framework on such boundaries.[46] Here, we tentatively provide a structural framework for justifying such mesopore arrangement. Whether the pore nucleating T-site is still uncertain, we suggest that the pore initiates at a prior point defect and during the steaming it grows by the very local coalescence of nearby newly formed point defects. However, we suppose that these nucleating sites of the newly formed mesopores are still invisible to tomography. Their presence, though, might be explained by the discrepancy between the mesoporous fraction obtained by N_2-physisorption and 3D TEM. In defect-poor crystal zones, the absence of propagation-directing structural features (for example grain boundaries) constrains the closed mesopores to an isotropic growth regime until reaching a critical size, without the further possibility to coalesce in anisotropic fashion. More recently, it was shown by DFT computation for the FAU and USY structure that defect sites (surface termination defect or point defect) are more

favorable for initiating the dealumination reaction than bulk non-defective sites.[47] Although the modeled defect sites are not structurally comparable to stacking faults, it is likely that bond distortion at a stacking fault will have comparable effects of facilitating dealumination. The localization of dealumination-related mesopores along stacking faults is therefore reasonable from a thermodynamic standpoint. However, a further analysis is required for corroborating *ab initio* the mechanism of pores formation and extraction of Al from the grains, accounting for which type of defects is more prone to bond breaking for the insertion of secondary pores.

Pore growth and coalescence. The ion exchange promotes another type of porosity, which in our study is identified as the intracrystalline channeling mesoporosity. Accordingly with the work of Sato and coworkers and contrarily to the general assumption, the three ionic exchange baths involve an extension of the mesopore system and a potential change in the structure of the zeolite.[48] It is thought that while the raise of V_μ could be imputed to the change of the cation, the increase in V_M is believed to be caused by washing the EFAL away. Although we do not completely exclude this hypothesis, we have observed a new category of mesopores with an increased volume at this stage: the elongated intracrystalline mesopores (together with the isolated mesopores and the surface roughness of Fig. 5c and d). The common peak at 7–8 nm of diameter in the PSD for both closed and open mesopores (Fig. 4c and d) may hint at the close relationship between these two classes of porosity. This hypothesis finds support in the reconstructed slice of the ionic exchange zeolite of Fig. 6, suggesting that the channeling mesopore is none other than a sequence of more regularly shaped isolated mesopores. Therefore, as it was previously presented in the pioneer works,[29,30] the open channeling mesopores are likely to derive from the closed cavity-like mesopores. In agreement with this research, we also claim that the introduction of the mesopores in Faujasite Y zeolites by following a typical dealumination pathway initially responds to a unique mechanism of lattice rearrangement to form isotropic cavities (or closed) mesopores. These cavities expand until reaching a size of 8 nm diameter, confirmed by the closed PSD of Fig. 4c. Beyond this critical size, the pore diameter stops growing, and the cavities start coalescing, where they are sufficiently populated, along discrete orientations typically within (111) planes. Such pore growth mechanism could also explain the peculiar necklace-like (instead of cylinder) morphology. As it is verified by the important volume fraction related to the very low sphericity class of porosity (Fig. S9), the channeling mechanism relays the isotropic pore growth regime. The constant increase of the mesoporous volume is ensured even after the second high temperature steaming and confirmed by both N_2 and 3D TEM. At this stage, the porous system evolves with the nucleation and coalescence of cavities-like mesopores (including the small mesopores invisible by 3D TEM), resulting in new isolated and channeling mesopores, as for the previous steps, and by reciprocal merging of channeling mesopores, leading to a truly connected mesopores network. When the channeling mesopores run from the middle of the lateral facet to the center of the zeolite, the trajectory is not totally linear and the mesopore shape is seemingly 'faceted'. Interestingly, when they run from the corner of the octahedron shaped zeolite to its center, the channeling mesopores are propagating along two intersecting planes of symmetry {111}. We suspect that defects such as twins or stacking faults might concentrate along these radial trajectories and, to minimize the mesopore surface energy, the pore coalescing may evolve along this 1D axis, generated by two intersecting defective (111)-type planes. Stacking faults are indeed known to be a very frequent structural defect in FAU crystals, and previous investigations of dealuminated FAU have recognized a correlation between stacking faults and channeling mesopore localization.[38] As it was reported by Karwacki and collaborators, the mesopore orientation is in fact symptomatic of the shortest way to restructure the lattice in order to remove the Al atoms of the framework.[49] This framework arrangement to include the mesopores can find an agreement in the XRD results reported in SI. The evolution of the lattice parameters and the changes in percentage of the crystallinity within the samples (Table S2), showing oscillating values, suggests the presence of amorphous material, in some extent correlated to the mechanism of mesoporisation. This hypothesis is corroborated by the physisorption results on the microporous volume, where the amorphous material possibly occluding the micropores, could explain the non-linear behavior of V_μ compared to V_M. The presence of such amorphous extra-framework phase that is generated during the dealumination, and in particular during the steaming, is also guessed in Fig. 6e and f. This material could be associated with a phase of higher density, particularly in the external crust and within the mesopores, where the ADF-STEM contrast differs from that of the typical microporous matrix. Furthermore, this finding aligns with the results of recent work that revealed the presence of a dense, segregated aluminosilicate phase.[50] Differently from the closed mesopores, the open channeling mesopore are characterized by a bimodal PSD according to 3D TEM measurements. The two populations of diameters refer to different morphological aspects of the same pore, instead of two distinct populations of mesopores. On one hand, the peak at 5 nm is assigned to the mesopore entries on the facet, to its constricted portions and to some minor branching. On the other hand, its main body is mainly described by the second broad population peaked at 13 nm. Compared to the previous treatment, even if the steaming 2 results in larger main body pore diameter, the necklace morphology leads to frequent bottlenecks. Finally, the regions where the channeling mesopores mutually converge are depicted by the tail of the PSD for $d >$ 20 nm. Therefore, while the isolated mesopores keep constant in size and in their total volume, corroborating the hypothesis of a pore nucleation mechanism that is constrained by a building block critical size of 8 nm, the channeling mesopores show a gradient in the diameters size from the facet to the center of the zeolite. As it was already evoked by Mehlhorn and coworkers,[17] the pore evolution is confined between crystalline domains and amorphous material around, acting like bound-

aries to its growth. Thus, it is plausible that the class of lower diameter in such a pore is caused by an accumulation of amorphous extra-framework material surrounding the pore, as the reader can observe in the outer surface of Fig. 6e and in the 3D representation of the pore size distribution in Fig. 5d, condition that is not verified in the core of the zeolite where larger diameters are attributed. To summarize, the steaming 2 not only creates closed mesopores but also digs into the core of the zeolite along radial directions on the (111) plane and enlarges the already existing open pores, while keeping the necklace-like pore configuration. The presence of extra-framework material as a collateral effect of the treatment is also accounted. Finally, the evolution of the intercrystalline mesoporosity was not recorded step-wise by 3D TEM since the selected crystals were chosen specifically to be bare of such complexity. The analysis by SEM, on the other hand, could incorporate the diversity in terms of grain morphologies along with the dealumination (Fig. S3), where we could appreciate the abundance of this type of mesoporosity between twinned crystals at every stage of the protocol.

Pore smoothing. The use of the acid in the last step of the dealuminating treatment leads to the final stage of the catalyst post-synthesis design. According to electron tomography, the channeling pore is here mainly characterized by a broad distribution of diameters that peak at 14 nm, however the pore mouths and a few constrictions justify the very little population of diameters at 5 nm. Larger diameters describing the void fraction, in this case around 27 nm, are found in the core of the zeolite. Despite the similarity of the PSD obtained by 3D TEM with the previous step of the dealumination, the channeling mesopore is here reshaped into a more regular cylinder. This is featured by a reduced bottlenecking effect, resulting in a diameter of 8 nm (contrarily to the 6 nm of the steaming 2). During the leaching, the mesopores are enlarged and their walls smoothed. The pore surface level off involves the removal of debris material, which is generated during the steaming and accumulates on the pore walls, and that could possibly obstruct the pore. Therefore, the rise of V_M that is registered at this stage is not necessarily associated to a direct creation of mesopores, but more to a morphological transformation of such preexisting pores and surface smoothing. It is important to stress that these results that address such specific factors would be difficult to obtain by other techniques than 3D TEM.

Implications for material design

For a single steamed Y zeolite, as it was claimed by Kortunov and collaborators,[51] the secondary pore system is just emerging. At this stage it occupies less than 3% of the total zeolite volume and does not form a percolation network, since it is basically constituted by isolated mesopores, intercrystalline mesopores and surface roughness. Therefore, the diffusion through the crystal must be assisted by micropores. The ion exchange represents a real turning point in the design of a mesoporous material, because the pore growth shifts from the isotropic to the anisotropic regime with the development of the intracrystalline channeling mesoporosity. The second hydrothermal treatment emphasizes the presence of channeling mesopores until building a truly connected mesoporous network that crosses the zeolite from edge to edge. This labyrinthic pore system is depicted in 3D in Fig. 5d and plays a key role in the diffusive properties of the material. Finally, the leaching represents a crucial passage in the catalyst preparation to obtain a highly efficient USY zeolite. This is achieved by removal of non-framework material, such as debris, originated from previous treatments and by reshaping the pores walls into smoothed cylinder-like morphologies. The access to the active sites on the surface and inside the zeolite is eased, and the material is ready to use for catalytic application.

Conclusions

This work provides mechanistic insight into the dealumination process used to design a highly stabilized USY zeolite starting from a Faujasite Y, by combining electron microscopy techniques, especially 3D TEM, with physisorption analysis. Through the collection of morphological descriptors, this study traces the evolution of the porous network all along the sequence of thermo-chemical treatments employed for a hierarchical catalyst preparation. The incorporation of mesopores inside the zeolite structure occurs at the expense of its intrinsic microporous matrix in response to a morphological and structural rearrangement inside the lattice. The first mesopores to be observed are isolated cavities-like mesopores on defective planes, typically stacking faults, together with irregularly shaped intercrystalline mesopores along the twinnings of the crystal. Further dealuminating treatments are needed for the development of the intracrystalline channeling mesoporosity. Their morphology, similar to a necklace instead of a truly cylinder, calls for a mechanism of coalescence of isolated mesopores on discretized directions of elongation, typically involving {111} planes. We also suggest that the variety of mesopores is caused by a heterogeneous concentration of defects. In particular, the twin intersections further focus the localization of structural dealumination, defect migration and mesopore stabilization. Meanwhile, the closed mesopores are believed to nucleate in crystal zones devoid of {111} twin planes and therefore remain isolated. Additionally, this study reports the achievement of a threshold pore diameter at the transition between an individual isotropic pore growth, typical of the isolated mesopores, and a migration-coalescence regime for the channelling mesopores. However, the role of the amorphous material on the mesopore size and the type of defects that is confined in the zeolite until the final leaching step remains unclear. These findings provide a dynamic structure-morphology framework that should foster the further optimization of USY heterogeneous catalysts.

Author contributions

Valentina Girelli Consolaro: investigation, formal analysis, data curation, conceptualization, writing – original draft,

writing – review & editing. Virgile Rouchon: supervision, data curation, conceptualization, writing – review & editing. Walid Baaziz: investigation, formal analysis, supervision, writing – review & editing. Adam Hammoumi: data curation, software. Tom Ferté: investigation, writing – review & editing. Gerhard Pirngruber: conceptualization. Maxime Moreaud: data curation, software, supervision, writing – review & editing. Ovidiu Ersen: data curation, conceptualization, supervision, visualization, validation, writing – review & editing.

Conflicts of interest

There are no conflicts to declare.

Data availability

The data supporting this article have been included as part of the SI. Videos of zeolites' reconstructions and surface renderings are also provided as supporting material. See DOI: https://doi.org/10.1039/d5nr01457c.

Acknowledgements

This work has been conducted in the framework of the Laboratoire Commun de Recherche Caractérisation des Matériaux pour les Energies Nouvelles (LCR CARMEN) and funded by IFP Energies Nouvelles (IFPEN). The authors would like to thank Dr C. Chizallet, Dr A. Lesage, Dr Z. Wang and Dr T. Jarrin for the fruitful discussions on the topic, and Dr. M. Dodin, A. Beaulieu and S. Lazare from IFPEN for their precious help in preparing the sample. The authors would also like to thank S. Humbert and P. Lecour for the XRD analysis, as well as the TEM and SEM platforms in IPCMS and IFPEN.

References

1 A. Corma, From Microporous to Mesoporous Molecular Sieve Materials and Their Use in Catalysis, *Chem. Rev.*, 1997, **97**(6), 2373–2420, DOI: 10.1021/cr960406n.
2 M. E. Davis, Zeolites and Molecular Sieves: Not Just Ordinary Catalysts, *Ind. Eng. Chem. Res.*, 1991, **30**(8), 1675–1683, DOI: 10.1021/ie00056a001.
3 B. A. Holmberg, H. Wang and Y. Yan, High Silica Zeolite Y Nanocrystals by Dealumination and Direct Synthesis, *Microporous Mesoporous Mater.*, 2004, **74**(1–3), 189–198, DOI: 10.1016/j.micromeso.2004.06.018.
4 K. P. de Jong, J. Zečević, H. Friedrich, P. E. de Jongh, M. Bulut, S. van Donk, R. Kenmogne, A. Finiels, V. Hulea and F. Fajula, Zeolite Y Crystals with Trimodal Porosity as Ideal Hydrocracking Catalysts, *Angew. Chem., Int. Ed.*, 2010, **49**(52), 10074–10078, DOI: 10.1002/anie.201004360.
5 M. Milina, S. Mitchell, N.-L. Michels, J. Kenvin and J. Pérez-Ramírez, Interdependence between Porosity, Acidity, and Catalytic Performance in Hierarchical ZSM-5 Zeolites Prepared by Post-Synthetic Modification, *J. Catal.*, 2013, **308**, 398–407, DOI: 10.1016/j.jcat.2013.08.020.
6 D. Verboekend and J. Pérez-Ramírez, Design of Hierarchical Zeolite Catalysts by Desilication, *Catal. Sci. Technol.*, 2011, **1**(6), 879–890, DOI: 10.1039/C1CY00150G.
7 K. Möller and T. Bein, Mesoporosity – a New Dimension for Zeolites, *Chem. Soc. Rev.*, 2013, **42**(9), 3689–3707, DOI: 10.1039/C3CS35488A.
8 Y. Wei, T. E. Parmentier, K. P. De Jong and J. Zečević, Tailoring and Visualizing the Pore Architecture of Hierarchical Zeolites, *Chem. Soc. Rev.*, 2015, **44**(20), 7234–7261, DOI: 10.1039/C5CS00155B.
9 J. Garcia-Martinez, C. Xiao, K. A. Cychosz, K. Li, W. Wan, X. Zou and M. Thommes, Evidence of Intracrystalline Mesostructured Porosity in Zeolites by Advanced Gas Sorption, Electron Tomography and Rotation Electron Diffraction, *ChemCatChem*, 2014, **6**(11), 3110–3115, DOI: 10.1002/cctc.201402499.
10 C. J. H. Jacobsen, C. Madsen, J. Houzvicka, I. Schmidt and A. Carlsson, Mesoporous Zeolite Single Crystals, *J. Am. Chem. Soc.*, 2000, **122**(29), 7116–7117, DOI: 10.1021/ja000744c.
11 A. Sachse and J. García-Martínez, Surfactant-Templating of Zeolites: From Design to Application, *Chem. Mater.*, 2017, **29**(9), 3827–3853, DOI: 10.1021/acs.chemmater.7b00599.
12 Z. Qin, G. Melinte, J.-P. Gilson, M. Jaber, K. Bozhilov, P. Boullay, S. Mintova, O. Ersen and V. Valtchev, The Mosaic Structure of Zeolite Crystals, *Angew. Chem., Int. Ed.*, 2016, **55**(48), 15049–15052, DOI: 10.1002/anie.201608417.
13 J. Van Aelst, M. Haouas, E. Gobechiya, K. Houthoofd, A. Philippaerts, S. P. Sree, C. E. A. Kirschhock, P. Jacobs, J. A. Martens, B. F. Sels and F. Taulelle, Hierarchization of USY Zeolite by NH4OH. A Postsynthetic Process Investigated by NMR and XRD, *J. Phys. Chem. C*, 2014, **118**(39), 22573–22582, DOI: 10.1021/jp5058594.
14 C. Marcilly, Les Zéolithes: Structures, Synthèse et Modifications, *Pet. Tech.*, 1986, **328**, 12–18.
15 M. C. Silaghi, C. Chizallet, J. Sauer and P. Raybaud, Dealumination Mechanisms of Zeolites and Extra-Framework Aluminum Confinement, *J. Catal.*, 2016, **339**, 242–255, DOI: 10.1016/j.jcat.2016.04.021.
16 J. Kenvin, S. Mitchell, M. Sterling, R. Warringham, T. C. Keller, P. Crivelli, J. Jagiello and J. Pérez-Ramírez, Quantifying the Complex Pore Architecture of Hierarchical Faujasite Zeolites and the Impact on Diffusion, *Adv. Funct. Mater.*, 2016, **26**(31), 5621–5630, DOI: 10.1002/adfm.201601748.
17 D. Mehlhorn, J. Rodriguez, T. Cacciaguerra, R.-D. Andrei, C. Cammarano, F. Guenneau, A. Gedeon, B. Coasne, M. Thommes, D. Minoux, C. Aquino, J.-P. Dath, F. Fajula and A. Galarneau, Revelation on the Complex Nature of Mesoporous Hierarchical FAU-Y Zeolites, *Langmuir*, 2018, **34**(38), 11414–11423, DOI: 10.1021/acs.langmuir.8b03010.
18 M. Milina, S. Mitchell, D. Cooke, P. Crivelli and J. Pérez-Ramírez, Impact of Pore Connectivity on the Design of

Long-Lived Zeolite Catalysts, *Angew. Chem., Int. Ed.*, 2015, **54**(5), 1591–1594, DOI: 10.1002/anie.201410016.

19 Z. Qin, S. Zeng, G. Melinte, T. Bučko, M. Badawi, Y. Shen, J.-P. Gilson, O. Ersen, Y. Wei, Z. Liu, X. Liu, Z. Yan, S. Xu, V. Valtchev and S. Mintova, Understanding the Fundamentals of Microporosity Upgrading in Zeolites: Increasing Diffusion and Catalytic Performances, *Adv. Sci.*, 2021, **8**(17), 2100001, DOI: 10.1002/advs.202100001.

20 J. Van Aelst, D. Verboekend, A. Philippaerts, N. Nuttens, M. Kurttepeli, E. Gobechiya, M. Haouas, S. P. Sree, J. F. M. Denayer, J. A. Martens, C. E. A. Kirschhock, F. Taulelle, S. Bals, G. V. Baron, P. A. Jacobs and B. F. Sels, Catalyst Design by NH4OH Treatment of USY Zeolite, *Adv. Funct. Mater.*, 2015, **25**(46), 7130–7144, DOI: 10.1002/adfm.201502772.

21 A. H. Janssen, H. Talsma, M. J. Van Steenbergen and K. P. De Jong, Homogeneous Nucleation of Water in Mesoporous Zeolite Cavities, *Langmuir*, 2004, **20**(1), 41–45, DOI: 10.1021/la034340k.

22 J. Kenvin, J. Jagiello, S. Mitchell and J. Pérez-Ramírez, Unified Method for the Total Pore Volume and Pore Size Distribution of Hierarchical Zeolites from Argon Adsorption and Mercury Intrusion, *Langmuir*, 2015, **31**(4), 1242–1247, DOI: 10.1021/la504575s.

23 I. C. Medeiros-Costa, C. Laroche, J. Pérez-Pellitero and B. Coasne, Characterization of Hierarchical Zeolites: Combining Adsorption/Intrusion, Electron Microscopy, Diffraction and Spectroscopic Techniques, *Microporous Mesoporous Mater.*, 2019, **287**, 167–176, DOI: 10.1016/j.micromeso.2019.05.057.

24 R. L. Volkov, V. N. Kukin, P. A. Kots, I. I. Ivanova and N. I. Borgardt, Complex Pore Structure of Mesoporous Zeolites: Unambiguous TEM Imaging Using Platinum Tracking, *ChemPhysChem*, 2020, **21**(4), 275–279, DOI: 10.1002/cphc.201901208.

25 I. Florea, L. Roiban, C. Hirlimann, F. Tihay, C. Pham-Huu, J. Werckmann, C. Pham, P. Nguyen, M. Drillon and O. Ersen, 3D–TEM Characterization of the Porosity in Nanoscaled Materials: Application to Catalysis, *Adv. Eng. Mater.*, 2011, **13**(3), 122–127, DOI: 10.1002/adem.201000220.

26 S. Bals, K. J. Batenburg, D. Liang, O. Lebedev, G. Van Tendeloo, A. Aerts, J. A. Martens and C. E. A. Kirschhock, Quantitative Three-Dimensional Modeling of Zeotile Through Discrete Electron Tomography, *J. Am. Chem. Soc.*, 2009, **131**(13), 4769–4773, DOI: 10.1021/ja8089125.

27 A. J. Koster, U. Ziese, A. J. Verkleij, A. H. Janssen and K. P. De Jong, Three-Dimensional, Transmission Electron Microscopy: A Novel Imaging and Characterization Technique with Nanometer Scale Resolution for Materials Science, *J. Phys. Chem. B*, 2000, **104**(40), 9368–9370, DOI: 10.1021/jp0015628.

28 K. Lee, S. Lee, Y. Jun and M. Choi, Cooperative Effects of Zeolite Mesoporosity and Defect Sites on the Amount and Location of Coke Formation and Its Consequence in Deactivation, *J. Catal.*, 2017, **347**, 222–230, DOI: 10.1016/j.jcat.2017.01.018.

29 A. H. Janssen, A. J. Koster and K. P. De Jong, Three-Dimensional, Transmission Electron Microscopic Observations of Mesopores in Dealuminated Zeolite Y, *Angew. Chem., Int. Ed.*, 2001, **40**(6), 1102–1104, DOI: 10.1002/1521-3773(20010316)40:6<1102::AID-ANIE11020>3.0.CO;2-6.

30 A. H. Janssen, A. J. Koster and K. P. De Jong, On, the Shape of the Mesopores in Zeolite Y: A Three-Dimensional Transmission Electron Microscopy Study Combined with Texture Analysis, *J. Phys. Chem. B*, 2002, **106**(46), 11905–11909, DOI: 10.1021/jp025971a.

31 J. Zečević, C. J. Gommes, H. Friedrich, P. E. de Jongh and K. P. de Jong, Mesoporosity of Zeolite Y: Quantitative Three–Dimensional Study by Image Analysis of Electron Tomograms, *Angew. Chem., Int. Ed.*, 2012, **51**(17), 4213–4217, DOI: 10.1002/anie.201200317.

32 D. Mastronarde, Tomographic Reconstruction with the IMOD Software Package, *Microsc. Microanal.*, 2006, **12**(S02), 178–179, DOI: 10.1017/S1431927606069467.

33 C. MessaoudiI, T. Boudier, C. O. S. Sorzano and S. Marco, TomoJ: Tomography Software for Three-Dimensional Reconstruction in Transmission Electron Microscopy, *BMC Bioinf.*, 2007, **8**(1), 288, DOI: 10.1186/1471-2105-8-288.

34 A. Fedorov, R. Beichel, J. Kalpathy-Cramer, J. Finet, J.-C. Fillion-Robin, S. Pujol, C. Bauer, D. Jennings, F. Fennessy, M. Sonka, J. Buatti, S. Aylward, J. V. Miller, S. Pieper and R. Kikinis, 3D Slicer as an Image Computing Platform for the Quantitative Imaging Network, *Magn. Reson. Imaging*, 2012, **30**(9), 1323–1341, DOI: 10.1016/j.mri.2012.05.001.

35 M. Moreaud, *Plug Im!*, 2016. https://www.plugim.fr/plugin/1.

36 C. A. Schneider, W. S. Rasband and K. W. Eliceiri, NIH Image to ImageJ: 25 Years of Image Analysis, *Nat. Methods*, 2012, **9**(7), 671–675, DOI: 10.1038/nmeth.2089.

37 V. Alfredsson, T. Ohsuna, O. Terasaki and J. Bovin, Investigation of the Surface Structure of the Zeolites FAU and EMT by High–Resolution Transmission Electron Microscopy, *Angew. Chem., Int. Ed. Engl.*, 1993, **32**(8), 1210–1213, DOI: 10.1002/anie.199312101.

38 Y. Sasaki, T. Suzuki, Y. Takamura, A. Saji and H. Saka, Structure Analysis of the Mesopore in Dealuminated Zeolite Y by High Resolution TEM Observation with Slow Scan CCD Camera, *J. Catal.*, 1998, **178**(1), 94–100, DOI: 10.1006/jcat.1998.2130.

39 J. C. Groen, L. A. A. Peffer and J. Pérez-Ramírez, Pore Size Determination in Modified Micro- and Mesoporous Materials. Pitfalls and Limitations in Gas Adsorption Data Analysis, *Microporous Mesoporous Mater.*, 2003, **60**(1–3), 1–17, DOI: 10.1016/S1387-1811(03)00339-1.

40 W. Wong-Ng, J. A. Kaduk, Q. Huang, L. Espinal, L. Li and J. W. Burress, Investigation of NaY Zeolite with Adsorbed CO2 by Neutron Powder Diffraction, *Microporous Mesoporous Mater.*, 2013, **172**, 95–104, DOI: 10.1016/j.micromeso.2013.01.024.

41 S. J. Blott and K. Pye, Particle Shape: A Review and New Methods of Characterization and Classification, *Sedimentology*, 2008, **55**(1), 31–63, DOI: **10.1111/j.1365-3091.2007.00892.x**.

42 S. Bernasconi, J. A. Van Bokhoven, F. Krumeich, G. D. Pirngruber and R. Prins, Formation of Mesopores in Zeolite Beta by Steaming: A Secondary Pore Channel System in the Plane, *Microporous Mesoporous Mater.*, 2003, **66**(1), 21–26, DOI: **10.1016/j.micromeso.2003.08.022**.

43 D. Fodor, A. Beloqui Redondo, F. Krumeich and J. A. Van Bokhoven, Role of Defects in Pore Formation in MFI Zeolites, *J. Phys. Chem. C*, 2015, **119**(10), 5447–5453, DOI: **10.1021/jp5117933**.

44 Z. Qin, W. Shen, S. Zhou, Y. Shen, C. Li, P. Zeng and B. Shen, Defect-Assisted Mesopore Formation during Y Zeolite Dealumination: The Types of Defect Matter, *Microporous Mesoporous Mater.*, 2020, **303**, 110248, DOI: **10.1016/j.micromeso.2020.110248**.

45 T. Ohsuna, O. Terasaki, D. Watanabe, M. W. Anderson and S. W. Carr, Dealumination of Hexagonal (EMT)/Cubic (FAU) Zeolite Intergrowth Materials: A SEM and HRTEM Study, *Chem. Mater.*, 1994, **6**(12), 2201–2204, DOI: **10.1021/cm00048a001**.

46 Z. Qin, B. Wang, N. Asano, L. Wang, Y. Zhou, X. Liu, B. Shen, S. Mintova, S. Asahina and V. Valtchev, Towards a Comprehensive Understanding of Mesoporosity in Zeolite Y at the Single Particle Level, *Inorg. Chem. Front.*, 2022, **9**(10), 2365–2373, DOI: **10.1039/D2QI00313A**.

47 T. Jarrin, T. De Bruin and C. Chizallet, Stability and Acidity of Sites at the External Surface and at Point Defects of Faujasite, *ChemCatChem*, 2023, **15**(3), e202201302, DOI: **10.1002/cctc.202201302**.

48 K. Sato, Y. Nishimura, N. Matsubayashi, M. Imamura and H. Shimada, Structural Changes of Y Zeolites during Ion Exchange Treatment: Effects of Si/Al Ratio of the Starting NaY, *Microporous Mesoporous Mater.*, 2003, **59**(2–3), 133–146, DOI: **10.1016/S1387-1811(03)00305-6**.

49 L. Karwacki, D. A. M. de Winter, L. R. Aramburo, M. N. Lebbink, J. A. Post, M. R. Drury and B. M. Weckhuysen, Architecture-Dependent Distribution of Mesopores in Steamed Zeolite Crystals as Visualized by FIB-SEM Tomography, *Angew. Chem., Int. Ed.*, 2011, **50**(6), 1294–1298, DOI: **10.1002/anie.201006031**.

50 Y. Kamimura, T. Kodaira, H. Yamada, N. Hiyoshi and A. Endo, Direct Visualization of the Dealumination Process on Zeolite Y: How Was the Mesoporous Architecture Formed?, *Chem. Mater.*, 2025, **37**(8), 2735–2748, DOI: **10.1021/acs.chemmater.4c03233**.

51 P. Kortunov, S. Vasenkov, J. Kärger, R. Valiullin, P. Gottschalk, M. Fé Elía, M. Perez, M. Stöcker, B. Drescher, G. McElhiney, C. Berger, R. Gläser and J. Weitkamp, The Role of Mesopores in Intracrystalline Transport in USY Zeolite: PFG NMR Diffusion Study on Various Length Scales, *J. Am. Chem. Soc.*, 2005, **127**(37), 13055–13059, DOI: **10.1021/ja053134r**.